Efficient extreme-ultraviolet multi-band high-order wave mixing in silica

Filippo Campi[1,*,+], Sylvianne D.C. Roscam Abbing[1,+], Zhuang-Yan Zhang[1], Maarten van der Geest[1], and Peter M. Kraus[1,*]

[1]Advanced Research Center for Nanolithography, Science Park 106, 1098 XG Amsterdam, The Netherlands
[+]these authors contributed equally to this work

ABSTRACT

Solid-state high harmonic generation (SSHHG) is a relatively recent,[1–4] non-destructive technique that offers new insight into the dynamics of strong-field light-matter interaction.[1–3,5–8] At the same time, SSHHG holds promise for being a viable route to engineering innovative, flexible, compact sources with emission in the extreme-ultraviolet (XUV) spectral range.[9,10] The technique has already been shown to yield XUV light,[3,11–13] albeit with low conversion efficiencies, as compared to the more traditional gas-based high harmonic generation (HHG) sources.[3,11] In this work we demonstrate that a non-collinear, multicolor SSHHG arrangement leads to spectra in the XUV with a high degree of tunability, and a considerable enhancement of the output flux. The observed behaviour can be understood in terms of perturbative optical wave mixing over more than one order of magnitude of the drive intensity. In addition, a model based on the recently-introduced injection current[8] allows accurate predictions over the entire experimental range.

Keywords: Solid-state high harmonic generation, wave mixing, non-collinear, extreme-ultraviolet light, femtosecond and attosecond pulses, ultrafast spectroscopy, ultrafast optics

1. INTRODUCTION

Wide-spread availability of lab-sized XUV sources based on HHG from gases has sparked significant progress in nanometer-scale imaging[16,17] and ultrafast spectroscopy.[14,15] As HHG finds its way into industrial applications,[18,19] the requirement to improve its conversion efficiency to levels that enable robust applications, has led to deeper understanding of how multi-color drivers increase the brightness of HHG sources.[19–23]

SSHHG is characterized by the choice of the driving field and generation material, which profoundly influence the generation mechanism. The leading causes for high-harmonic emission from solids discussed in the literature are on the one hand nonlinear intraband currents, that are created by strong-field carrier acceleration following excitation at the Γ-point,[1,3] and on the other hand electron-hole recollisions after carrier acceleration away from the Γ-point.[2,5] More recently, it has been shown that the excitation step itself gives rise to a nonlinear current, referred to as injection current, which results in harmonic emission from silica.[8] We note that a quantum mechanical, few-level dynamics description of SSHHG should contain such injection currents, which may thus be implicitly contained in previous studies, such as the experimental and theoretical investigations of HHG from solid rare gases.[24–26]

The observation of enhanced conversion efficiency of gas HHG for short-wavelength drivers[27] suggests a strategy for enhancing SSHHG. The combination of multi-wavelength drivers and a non-collinear arrangement employed in the present work is shown to lead to a high degree of spectral tunability, while increasing the overall flux by more than one order of magnitude. While a quantum-mechanical model simulating a strongly-driven population exchange between a few levels fully reproduces the experimental observations, the overall behavior can be intuitively understood within the framework of perturbative optical wave mixing over a wide range of experimental parameters.

International Conference on X-Ray Lasers 2020, edited by Davide Bleiner,
Proc. of SPIE Vol. 11886, 118860G · © 2021 SPIE · CCC code:
0277-786X/21/$21 · doi: 10.1117/12.2593359

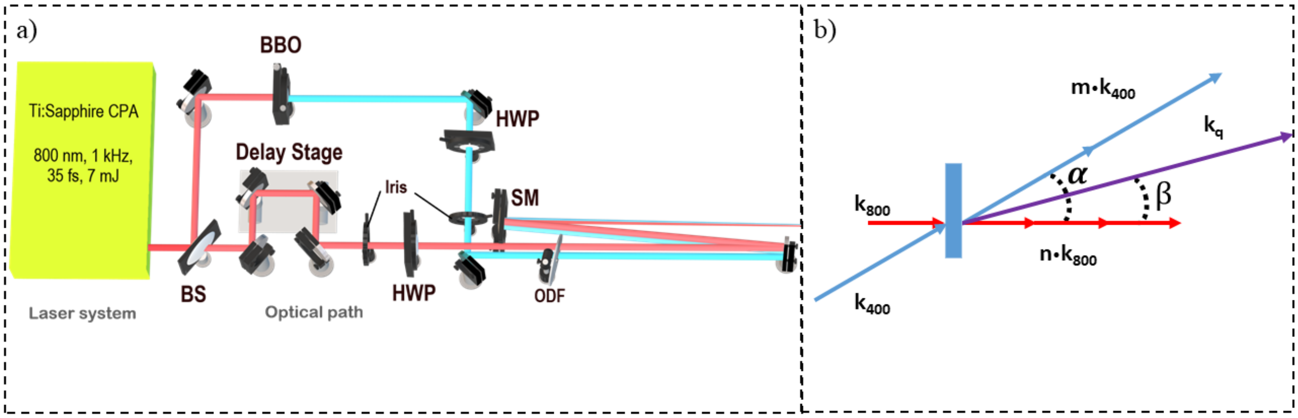

Figure 1. a) Top view of the experimental setup. BS: beam splitter, HWP half-waveplate, SM: spherical mirror. The portion of the fundamental not converted into second harmonic is removed by means of dichroic mirrors. b) Schematic representation of wave mixing in the silica sample. The crossing angle α is determined by the spatial separation of the two parallel beams onto the spherical mirror, and its focal length. The emission angle β is given by $\beta(n, m) = \frac{2m \sin\alpha}{n+2m\cos\alpha}$, where n and m are the numbers of 800 nm and 400 nm photons involved in the wave mixing process.

2. EXPERIMENT

Figure 1a shows the experimental setup from the top view, and Figure 1b is a schematic representation of wave mixing in the silica sample. The output of a Ti:sapphire amplifier (Coherent Astrella, 800 nm, 1 kHz) is split into two arms. In one arm, the second harmonic is generated inside a β-barium borate (BBO) crystal. The second arm includes a delay line to optimize synchronization of the two pulses onto the sample. Half waveplates are placed in both arms to ensure parallel relative polarization of the pulses. Focusing is achieved by means of a spherical mirror with focal length f=500 mm. The crossing angle of 17.5 mrad in focus is implemented by impinging onto the spherical mirror with the two beams parallel and displaced in height by 9 mm. The beam sizes are individually adjusted so as to maximize the signal while preventing damaging the sample. This leads to the area of the focal distribution of the second harmonic to be half the size of the fundamental. The generated harmonics are spectrally dispersed along the horizontal direction with an aberration-corrected, concave, flat-field grating (1200 lines/mm) and detected by a double-stack micro-channel plate assembly, backed with a phosphor screen, which is imaged with a CMOS camera from outside the vacuum chamber.

3. RESULTS AND DISCUSSION

Similarly to high-order wave mixing experiments in gases,[28, 29] the angle between fundamental (800 nm) and second harmonic (400 nm) driving pulses (Figure 1b) provides an angular separation of all photon channels and prevents their overlap and interference, unlike in collinear two-color HHG.[30] The non-collinear configuration yields an emission pattern (Figure 1b) of harmonic wave mixing orders (WMOs) labeled (n, m), which obeys momentum conservation, and can be described by vectorial addition/subtraction of the wave vectors of n fundamental and m second-harmonic photons. Only combinations of an odd total number of photons are dipole-allowed due to the centrosymmetry of amorphous silica.

A typical emission pattern is shown in Figure 2. The propagation angle of the fundamental pulse defines the optical axis, while the propagation angle of the second harmonic pulse is indicated with a dotted line at 17.5 mrad. Apart from harmonic orders resulting from a combination of odd photons from a single color, all the remaining HOs are well separated in the far field, and every photon combination is uniquely mapped onto its propagation angle, since the overall spectrum contains less than one octave.

In order to assess the suitability of the system as an XUV source, we performed a series of experiments aimed at characterizing the behavior of the yield as a function of driving intensities, shown in in Figure 3. Figure 3a and Fig. 3b display the emission intensity of harmonic orders as a function of the 400 nm and 800 nm intensity,

---

*f.campi@arcnl.nl; **p.kraus@arcnl.nl

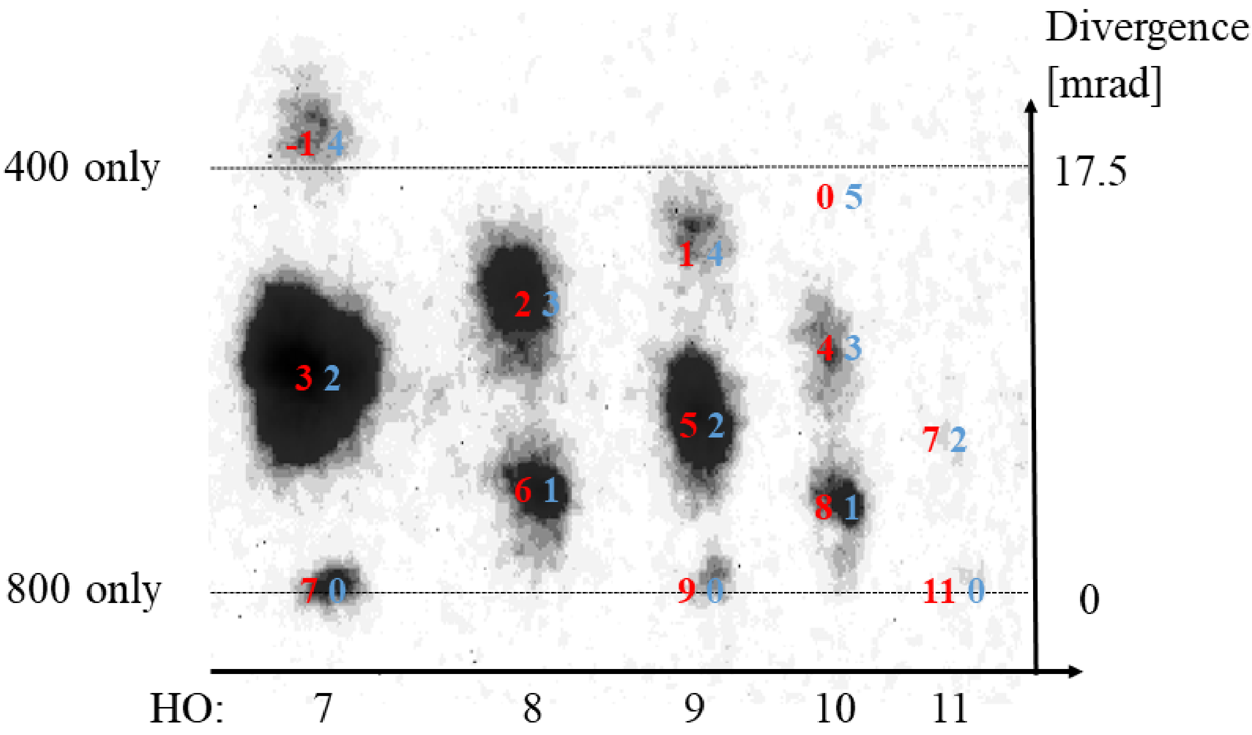

Figure 2. Typical far-field spectrum. Harmonic orders are labeled according to the notation introduced in the text. HO: harmonic order

respectively, while keeping the intensity of the other pulse constant. Figure 3c shows a scaling where the intensity of both pulses was scaled simultaneously, so as to keep their ratio constant. The open circles are experimental points, and the dashed lines represent power-laws consistent with a perturbative process with order equal to the number of photons of the pulse(s) whose intensity is scaled.

In order to verify the measured yields and intensity scalings, we solved the time-dependent Schroedinger equation for a three-level system. The energy spacing of the levels resembles the band structure of silica at the band gap (0 eV, 9 eV, and 13 eV for valence and the first two conduction bands, respectively).[31] The time-dependent coefficients associated with the eigenstates of the system give access to the temporal evolution of the individual populations of the states. The transfer of population between these states gives rise to a time-dependent, laser-induced current, which resembles an ionization/injection current.[31]

Figure 3 shows the yield of a number of harmonic orders, as a function of driving intensities. The solid lines are the output of our simulations, and the open circles are experimental data. The dashed lines are a visual guide, showing regions wherein the trend can be approximated by a power law with the exponent indicated by the labels, and consistent with the order of the process.

The comparison between experimental data and simulations presented in Figure 3 shows that a model based on a three-level system reproduces the data well, especially at high intensities, where the yield is well above the detection threshold. All curves show a slow initial rise, followed by a regime wherein the behaviour resembles that of a perturbative process (the curves approach a straight line in log-log scale). As the intensity approaches the damage threshold (experimentally estimated to be around 30 TW/cm^2) emission begins to saturate. This is not captured in our simulations as high intensity processes require the contribution from multiple higher bands and continuum states.

Overall, the theoretical predictions follow the experimental trends over more than one order of magnitude of the driving intensity. As it can be seen from Figure 3c, the intensity behavior of WMOs that arise from the

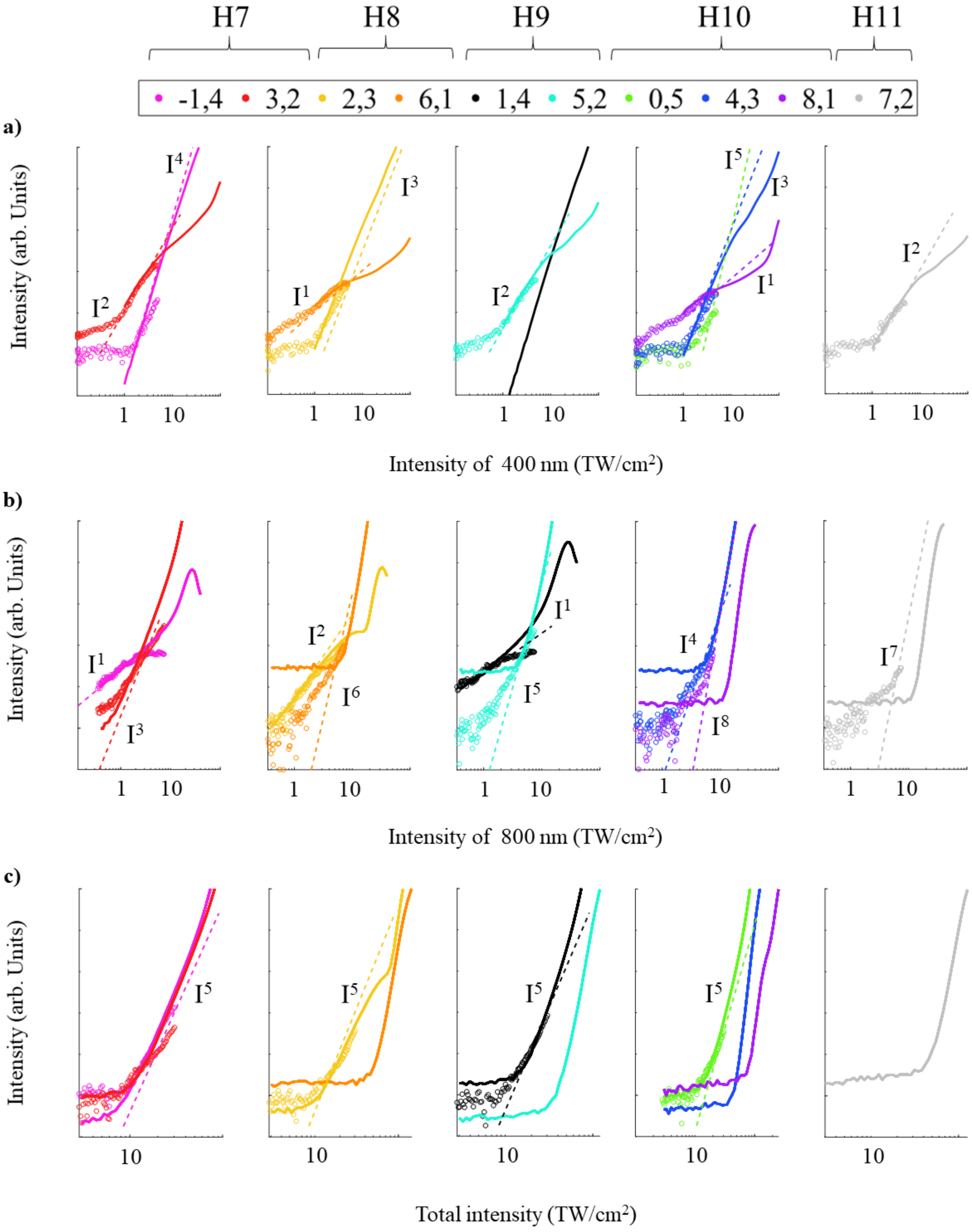

Figure 3. Intensity-dependent yield of various harmonic orders, sorted by photon energy. a) Only the intensity of the 400 nm pulse is scaled (the ratio I_{400}/I_{800} varies between 0.01:1 to 0.4:1 from left to right on the horizontal intensity axis, I_{800}=11.0 TW/cm^2. b) Only the intensity of the 800 nm pulse is scaled (the ratio I_{800}/I_{400} varies between 0.06:1 to 1.4:1 from left to right on the horizontal intensity axis, I_{400}=5.5 TW/cm^2). c) The total intensity of two colors is scaled (the ratio I_{400}/I_{800} is 4.3:1). The color coding is consistent across the panels. The error bars in the determination of the intensity were calculated to be 30%.

combination of five photons resembles strikingly that of a perturbative wave mixing process. If we turn now to the partial intensity scalings shown in panels a and b, it is clear that orders containing fewer photons of the color that is being scaled, are those that match the theoretical predictions best.

While a rigorous quantum-mechanical model can capture more experimental features, a consistent, perturbative-like behavior offers an intuitive experimental knob to adjust the emission patterns, thus offering tunability. Figures 4a and 4b show an example of such tunability. The two panels are far-field spectra obtained under nearly opposite illumination conditions. The former is recorded when 400 nm contributes to about 80% of the total intensity, and the center of mass of the emission is close to the optical axis defined by the propagation direction of the 400 nm pulses. The latter is instead recorded when the 800 nm pulses contribute about 70% of the total intensity. Hence, the center of mass of the distribution is closer to the optical axis defined by the propagation direction of the 800-nm pulses.

The good agreement between experiments and a qualitative perturbative behavior has important implications for XUV sources based on solid HHG. WMOs that are composed of a lower number of photons than the harmonics generated by the fundamental alone can be made much more efficient than one-color solid HHG.

To quantify the enhancement in the yield of specific harmonic orders, it is useful to compare yields across scans. We consider harmonics (7,0), (9,0), and (11,0) recorded while increasing the intensity of the 400 nm. Their yield does not increase with increasing intensity, since no 400 nm photons are involved in their generation. The yield of harmonic orders (3,2), (5,2), and (7,2) is then extracted from a scan wherein the intensity of the 800 nm is scaled. At a certain point during the scan, the total driving intensity of the two scans is matched. By calculating the ratio between the yield at this experimental point, it is possible to extract an enhancement factor. Figure 5 shows this analysis: the enhancement is larger than two orders of magnitude for H7 and H9, and larger than one order of magnitude at H11.

The non-collinear wave mixing technique enables the selective enhancement of individual or a selection of WMOs. At the same time the natural angular separation of WMOs renders spectral filtering by means of metallic foils unnecessary, which ultimately increases the available flux in the experiments.

These advantages allow for a bright and flexible source, which can be tuned to generate a single harmonic order, or a few orders. Even more control over the radiation can be exerted when generating XUV in crystalline quartz (Figure 6a), where the broken inversion symmetry enables emission pathways with an even total number of photons resulting in a much denser emission pattern. In Figure 6a, WMOs corresponding to an even number of photons are consistently weaker than those corresponding to an odd number. In addition, each energy is dominated by a single WMO, while all energies are still equally present in the emission but separated in emission angle.

When this generation scheme is applied, a number of different emission channels can be individually selected. By implementing angular separation in an optical setup, able to deliver single-color, femtosecond pulses (or shorter) for, e.g. pump-probe experiments in a spectral range that would otherwise be challenging to cover and isolate with traditional gas-HHG sources.

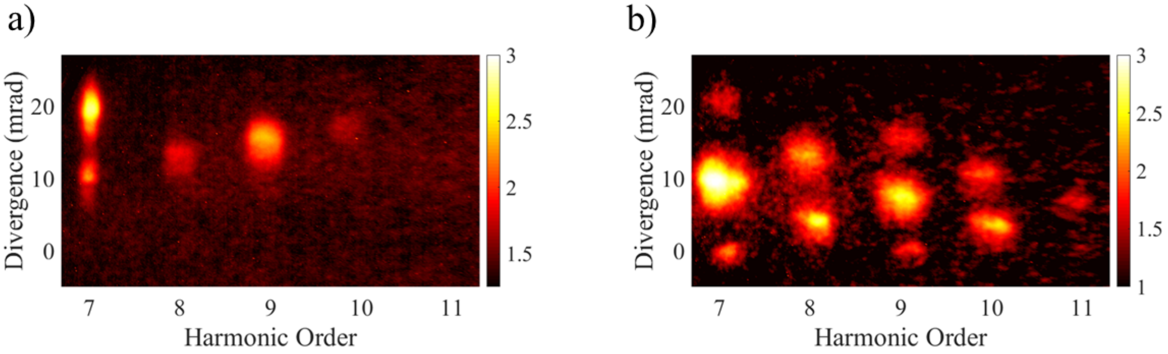

Figure 4. Far-field patterns, resolved in photon energy. a,b) Experimental spectra recorded at the highest intensity point of the plots in Figure 3a and 3b.

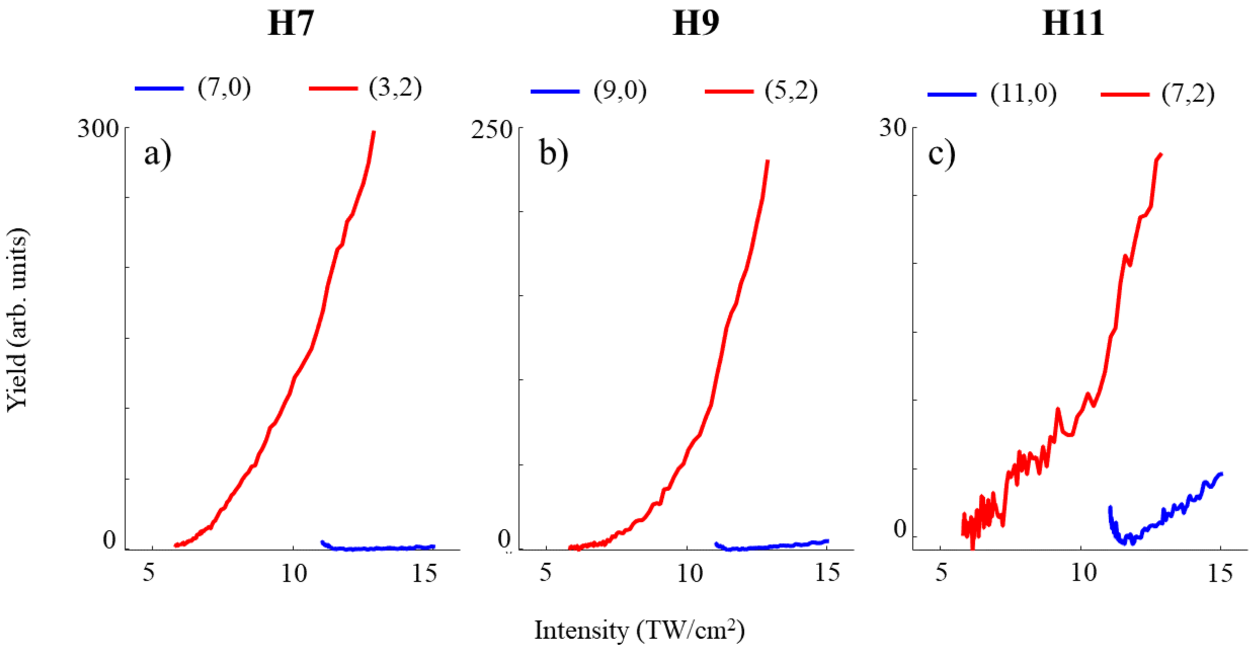

Figure 5. Comparison between the yield of an WMO and a single-color harmonic order, at the same photon energy and for different energies. The ratio between the red and the blue curves at the intensity point where the blue curves start is defined as the enhancement factor discussed in the text. a) Harmonics (7,0) and (3,2): 10.5 eV. b) Harmonics (9,0) and (5,2): 13.5 eV. c) Harmonics (11,0) and (7,2): 16.5 eV.

Another prospect shown in Figure 6b: by carefully adjusting the intensities of both beams, conditions can be found where a single WMO ((3,2) at an energy of harmonic order 7 (10.5 eV) dominates the emission pattern and is up to two orders of magnitude brighter than the other orders.

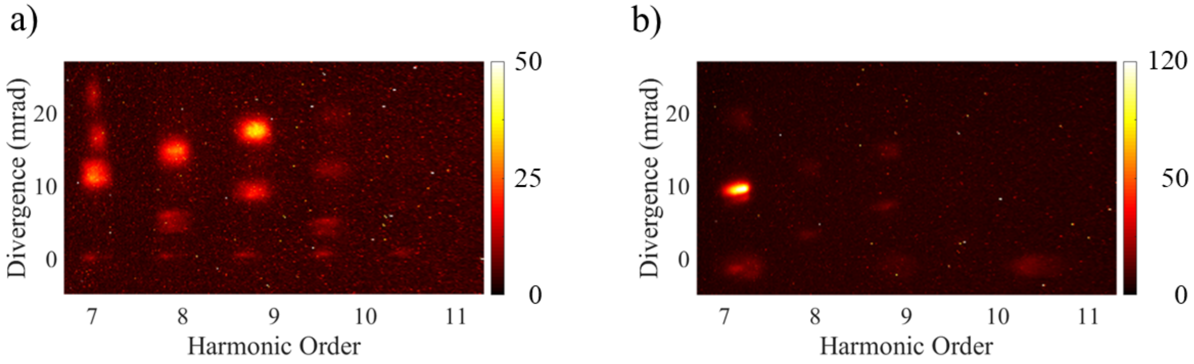

Figure 6. Far-field patterns, resolved in photon energy. c) Experimental far-field emission pattern generated in a crystalline quartz sample for I_{800}=11.6 TW/cm^2 and I_{400}=16.4 TW/cm^2. WMOs resulting from odd combinations of photons are consistently stronger than those arising from an even number of photons. d) Spectrum for I_{800}=12.8 TW/cm^2 and I_{400}=2.5 TW/cm^2.

4. CONCLUSIONS

We have shown that solid-state HHG in silica, driven by a femtosecond pulse and its second harmonic, overlapped in the sample at a small angle, yields rich emission patterns. Every emission channel arises from a unique combination of photons from the driving pulses, and has a characteristic propagation direction, thus providing intrinsic spatial separation of different photon energies. The intensity-dependent behaviour of each harmonic order can be fully captured by a model describing an injection current between three levels. This intensity scaling can also be approximated to a perturbative process, over a large range of intensities, thus providing an intuitive framework. The addition of the second harmonic, which lowers the total number of photons involved, renders wave mixing orders more efficient by at least one order of magnitude. This observation, together with the flexibility provided by our scheme, lays the ground for the development of compact and bright XUV sources (see also Sect. and Sect. 2 [35]).

REFERENCES

[1] Ghimire, S. et al. Observation of high-order harmonic generation in a bulk crystal, *Nat. Phys.* **2**, 138-141 (2011).

[2] Schubert, O. et al. Sub-cycle control of terahertz high-harmonic generation by dynamical Bloch oscillations, *Nat. Photonics* **8**, 119-123 (2014).

[3] Luu, T. T. et al. Extreme ultraviolet high-harmonic spectroscopy of solids, *Nature* **521**, 498-502 (2015).

[4] Golde, D., Meier, T., and Koch, S. W. High harmonics generated in semiconductor nanostructures by the coupled dynamics of optical inter- and intraband excitations, *Physical Review B* **77**, 075330 (2008).

[5] Vampa, G. et al. Linking high harmonics from gases and solids, *Nature* **522**, 462-464 (2015).

[6] Yoshikawa, N., Tamaya, T., and Tanaka, K. High-harmonic generation in graphene enhanced by elliptically polarized light excitation, *Science* **356**, 736 (2017).

[7] Hafez, H. A., et al. Extremely efficient terahertz high-harmonic generation in graphene by hot Dirac fermions, *Nature* **561**, 507 (2018).

[8] Jürgens, P. et al. Origin of strong-field-induced low-order harmonic generation in amorphous quartz, *Nat. Phys.* **16**, 1035-1039 (2020).

[9] Sivis, M. et al. Tailored semiconductors for high-harmonic optoelectronics, *Science* **21**, 357 (2017).

[10] Franz, D. et al. All semiconductor enhanced high-harmonic generation from a single nanostructured cone, *Sci. Rep.* **9**, 5663 (2019).

[11] Luu, T. T., Cagnoli, V. S., Saha, S. U., Heyderman, L. J., and Wörner, H. J. Generation of coherent extreme ultraviolet radiation from α– quartz using 50 fs laser pulses at a 1030 nm wavelength and high repetition rates, *Opt. Lett.* **43**, 1790-1793 (2018).

[12] Kim, H., et al. Extraction of higher-order nonlinear electronic response in solids using high harmonic generation, *Nat. Comm.* **10**, 3272 (2019).

[13] Uzan, A. J., et al. Attosecond spectral singularities in solid-state high-harmonic generation, *Nat. Phot.* **14**, 183 (2020).

[14] Kraus, P. M. and Wörner, H. J. Perspectives of attosecond spectroscopy for the understanding of fundamental electron correlations, *Angew. Chemie Int. Ed.* **57**, 5228-5247 (2018).

[15] Kraus, P. M., Zürch, M., Cushing, S. K., Neumark, D. M., and Leone, S. R. The ultrafast X-ray spectroscopic revolution in chemical dynamics, *Nat. Rev. Chem.* **2**, 82 (2018).

[16] Miao, J., Ishikawa, T., Robinson, I. K., and Murnane, M. M. Beyond crystallography: Diffractive imaging using coherent X-ray light sources, *Science* **348**, 530-535 (2015).

[17] Witte, S., Tenner, V. T., Noom, D. W. E., and Eikema, K. S. E. Lensless diffractive imaging with ultra-broadband table-top sources: from infrared to extreme-ultraviolet wavelengths, *Light. Sci. Appl.* **3**, e163 (2014).

[18] Ku, Y.-S. et al. EUV scatterometer with a high-harmonic-generation EUV source, *Opt. Express* **24**, 28014 (2016).

[19] Roscam Abbing, S. et al. Divergence Control of High-Harmonic Generation, *Phys. Rev. Appl.* **13**, 054029 (2020).

[20] Kim, I. J. et al. Highly efficient high-harmonic generation in an orthogonally polarized two-color laser field, *Phys. Rev. Lett.* **94**, 243901 (2005).

[21] Brizuela, F. et al. Efficient high-order harmonic generation boosted by below-threshold harmonics, *Sci. Rep.* **3**, 1410 (2013).

[22] Haessler, S. et al. Optimization of Quantum Trajectories Driven by Strong-Field Waveforms, *Phys. Rev. X* **4**, 021028 (2014).

[23] Rajeev, R. et al. In situ frequency gating and beam splitting of vacuum- and extreme-ultraviolet pulses, *Light Sci. Appl.* **5**, e16170 (2016).

[24] Wu, M., Ghimire, S., Reis, D. A., Schafer, K. J., and Gaarde, M. B. High-harmonic generation from Bloch electrons in solids, *Phys. Rev. A* **91**, 043839 (2015).

[25] Wu, M., Browne, D. A., Schafer, K. J., and Gaarde, M. B. Multilevel perspective on high-order harmonic generation in solids, *Phys. Rev. A* **94**, 063403 (2016).

[26] Ndabashimiye, G. et al. Solid-state harmonics beyond the atomic limit, *Nature* **534**, 520-523 (2016).

[27] Lai, C.-J. et al. Wavelength scaling of high harmonic generation close to the multiphoton ionization regime, *Phys. Rev. Lett.* **111**, 073901 (2013).

[28] Bertrand, J. B. et al. Ultrahigh-order wave mixing in noncollinear high harmonic generation, *Phys. Rev. Lett.* **106**, 023001 (2011).

[29] Heyl, C. M. et al. Macroscopic Effects in Noncollinear High-Order Harmonic Generation, *Phys. Rev. Lett.* **112**, 143902 (2014).

[30] Li, L. et al. Scaling law of high harmonic generation in the framework of photon channels, *Phys. Rev. Lett.* **120**, 223203 (2018).

[31] Campi, F. manuscript in preparation.

[32] Kraus, P. M. et al. Measurement and laser control of attosecond charge migration in ionized iodoacetylene, *Science* **350**, 790-795 (2015).

[33] Silva, R. E. F., Blinov, I. V., Rubtsov, A. N., Smirnova, O., and Ivanov, M. High-harmonic spectroscopy of ultrafast many-body dynamics in strongly correlated systems, *Nat. Phot.* **12**, 266 (2018).

[34] Lakhotia, H., Kim, H. Y., Zhan, M., Hu, S., Meng, S., and Goulielmakis, E.. Laser picoscopy of valence electrons in solids, *Nature* **583**, 55-59 (2020).

[35] D. Bleiner, The Science and Technology of X-ray Lasers: A 2020 Update Proc. SPIE 11886, 1188602 (2021)